Transnational University Limburg is a unique collaboration of two universities in two countries: the University of Hasselt and Maastricht University.

UHASSELT
KNOWLEDGE IN ACTION

www.uhasselt.be
Universiteit Hasselt
Campus Hasselt:
Martelarenlaan 42 | 3500 Hasselt
Campus Diepenbeek:
Agoralaan Gebouw D | 3590 Diepenbeek

UHASSELT
KNOWLEDGE IN ACTION

Maastricht University

Faculty of Medicine and Life Sciences
School for Life Sciences
Master of Biomedical Sciences

Master's thesis

Validation of the Chimeric Fluorescent Reporter mClYFP-GlyR2 for Nanoscale Activity Mapping of the Glycine Receptor alpha2

Amber Van Bocxlaer

Thesis presented in fulfillment of the requirements for the degree of Master of Biomedical Sciences, specialization Molecular Mechanisms in Health and Disease

SUPERVISOR :
Prof. dr. Bert BRONE

MENTOR :
Mevrouw Yana VELLA

2024
2025

UHASSELT
KNOWLEDGE IN ACTION

Maastricht University

Faculty of Medicine and Life Sciences
School for Life Sciences
Master of Biomedical Sciences

Master's thesis

Validation of the Chimeric Fluorescent Reporter mClYFP-GlyR2 for Nanoscale Activity Mapping of the Glycine Receptor alpha2

Amber Van Bocxlaer

Thesis presented in fulfillment of the requirements for the degree of Master of Biomedical Sciences, specialization Molecular Mechanisms in Health and Disease

SUPERVISOR :

Prof. dr. Bert BRONE

MENTOR :

Mevrouw Yana VELLA

Validation of the Chimeric Fluorescent Reporter mClYFP-GlyRα2 for Nanoscale Activity Mapping of the Glycine Receptor alpha2*

Amber Van Bocxlaer[1], Yana Vella[1], and Bert Brône[1]

[1]Neurophysiology Lab, Biomedical Research Institute, Universiteit Hasselt, Campus Diepenbeek, Agoralaan Gebouw C - B-3590 Diepenbeek, Belgium

*Running title: *Validation of mClYFP-GlyRα2 for Activity Mapping*

To whom correspondence should be addressed: Prof. Dr. Bert Brône, Tel: +32 (11) 26 92 37; Email: bert.brone@uhasselt.be

Keywords: Glycine receptor alpha 2 (GlyRα2), fluorescent activity reporter, nanoscale activity mapping, subcellular localization, single-channel patch clamp, live-cell imaging

ABSTRACT

Maintaining excitation/inhibition (E/I) balance is essential for accurate information processing in the central nervous system, and disruption of this balance is implicated in psychiatric and neurological disorders, including psychosis and Parkinson's disease. Glycine receptors (GlyRs), ligand-gated chloride channels that modulate neuronal excitability, play a key role in maintaining E/I balance. Their effects are highly context-dependent and shaped by their cell-type-specific distribution across subcellular compartments. Elucidating their subcellular localization is therefore crucial for understanding their role in (patho)physiological contexts and for developing targeted therapies. To address the lack of suitable tools for such investigations, a chimeric fluorescent reporter, mClYFP-GlyRα2, was developed by fusing the GlyRα2 subunit to a yellow fluorescent chloride-sensor (mClYFP). This tool enables high-resolution live-cell imaging of GlyRα2 localization while simultaneously reporting receptor activity by detecting chloride flux. This study aims to validate mClYFP-GlyRα2 for nanoscale activity mapping of GlyRα2. Single-channel patch-clamp recordings demonstrated that the chimeric protein retains native ion channel properties, with unitary conductance comparable to wild-type GlyRα2. Live-cell TIRF imaging confirmed that mClYFP preserves its chloride-sensing functionality when fused to GlyRα2 and enables real-time, nanoscale, fluorescence-based detection of receptor activation. These findings validate mClYFP-GlyRα2 as a reliable dual-purpose tool for investigating the subcellular localization and nanoscale activity of GlyRα2 in living cells. Its application will advance our understanding of GlyRα2's modulatory role in diverse (patho)physiological contexts and support the development of targeted therapies aimed at restoring E/I balance. Furthermore, the design offers a blueprint for developing similar reporters for other Cys-loop receptors involved in E/I regulation.

INTRODUCTION

Proper functioning of the central nervous system (CNS) relies on a delicate balance between excitatory and inhibitory neurotransmission (1). This excitation/inhibition (E/I) balance is crucial for maintaining neuronal network stability and ensuring accurate information processing (2, 3). Disruption of E/I balance leads to abnormal neuronal signaling and is associated with various psychiatric and neurological disorders, including autism, schizophrenia, epilepsy, dementia, and Parkinson's disease (PD) (1-4). A key mechanism for preventing excessive excitation and maintaining E/I balance is fast inhibitory neurotransmission, primarily mediated by γ-aminobutyric acid type A receptors ($GABA_ARs$) and glycine receptors (GlyRs) (5-8). Consequently, these receptors have been suggested as important therapeutic targets for restoring E/I balance in different pathophysiological contexts (6, 9). Given their complex involvement in both the developing and adult CNS, and their therapeutic relevance, it is crucial to gain a deeper understanding of how they

modulate neuronal excitability in different physiological and pathophysiological contexts.

GlyRs are pentameric, ligand-gated chloride (Cl^-) channels belonging to the Cys-loop receptor family, composed of five subunits arranged symmetrically around a central ion-conducting pore (9, 10). Each subunit shares a conserved structure comprising a long extracellular N-terminus, four transmembrane domains (TM1-TM4), an intracellular loop between TM3 and TM4, and a short extracellular C-terminus (9-11).

These membrane-embedded receptors modulate neuronal excitability by controlling the flow of Cl^- ions across the neuronal membrane (5, 7, 12-15). Agonist binding to the extracellular site triggers rapid opening of the Cl^- permeable channel, increasing Cl^- conductance and shifting the membrane potential towards the Cl^- equilibrium potential (13-15). Whether this increases or decreases neuronal excitability depends on the direction of passive Cl^- flux, determined by the transmembrane Cl^- gradient and the membrane potential (16, 17).

In mature neurons, intracellular Cl^- concentration is kept low, resulting in an inward flow of Cl^- upon receptor activation and a reduction of neuronal excitability (5, 14-16, 18). This occurs through either hyperpolarization, which moves the membrane potential further from the action potential (AP) threshold, or shunting inhibition, where increased membrane conductance reduces the amplitude of excitatory postsynaptic potentials (EPSPs) (5, 16-19). Both mechanisms increase the amount of excitatory input required to trigger an AP, thereby helping to prevent excessive excitation and maintain E/I balance. Consequently, GlyRs are generally known as inhibitory receptors (13, 15). Interestingly, activation of these receptors can also be depolarizing, and even excitatory, in the developing brain and certain mature neurons, due to differences in Cl^- transporter expression (11, 14, 16). However, their modulatory effects are highly context-dependent, shaped not only by the transmembrane Cl^- gradient and membrane potential, but also by their subcellular localization and timing of receptor activation (18, 20).

GlyRs act at different subcellular compartments of neurons - Neurons are the largest and most morphologically complex cells of our body, containing multiple subcellular compartments, including the soma, dendritic shafts and spines, the axon initial segment (AIS), as well as synaptic and extrasynaptic regions, each playing a specialized role in neuronal function (21). How GlyRs modulate neuronal excitability is influenced by their cell type-specific distribution across these subcellular compartments.

Whether the receptor is located at synaptic or extrasynaptic sites determines its exposure to neurotransmitters and, consequently, how it modulates neuronal excitability (22, 23). Receptors located at postsynaptic sites are exposed to rapid presynaptic neurotransmitter release, resulting in fast, phasic (short) modulation (6, 23, 24). In contrast, receptors at extrasynaptic sites are exposed to lower levels of slowly diffusing neurotransmitters arising from paracrine release or spillover from the synaptic cleft, resulting in slow, tonic (sustained) modulation (6, 11, 23, 24).

Synaptic and extrasynaptic GlyRs are optimally adapted to their specific neurotransmitter environments. Synaptic receptors display fast activation and desensitization kinetics, allowing them to respond efficiently to transient, high-concentration neurotransmitter pulses released from presynaptic terminals (11, 24). In contrast, extrasynaptic receptors exhibit slower activation and desensitization kinetics and higher agonist sensitivity, making them well adapted to respond to lower, more sustained neurotransmitter levels (6, 11, 24). These functional differences are likely due to variations in subunit composition (11, 24). Functional GlyRs can exist as homopentamers, composed of five agonist-binding α-subunits, or as heteropentamers, consisting of four α-subunits and one β-subunit (24). The β-subunit facilitates synaptic localization by binding to the scaffolding protein gephyrin. This allows heteromeric GlyRs to cluster at post-synaptic sites, whereas homomeric GlyRs, lacking the β-subunit, are generally found at extrasynaptic sites (24, 25).

The subcellular localization of GlyRs also encompasses their distribution across distinct neuronal compartments such as the soma, dendritic shafts and spines, and the AIS (22). Each of these compartments plays a specific role in synaptic integration and AP generation (18). The precise positioning of receptors within these compartments determines their spatial relationship to excitatory inputs and the site of AP initiation. This influences whether they modulate the amplitude and propagation of EPSPs or alter the AP threshold, affecting the precision and strength of their modulatory effects (16, 17, 20, 22).

In dendrites, which receive synaptic inputs, GlyRs are ideally positioned to locally modulate incoming excitatory inputs (18, 26). Their proximity to excitatory synapses allows them to shunt EPSPs directly, attenuating their amplitude and propagation. This local modulation delays AP onset without affecting AP threshold (20). Receptors located at the soma, where converging dendritic inputs are integrated, exert broader control over neuronal output by modulating EPSP summation (18). Their activation induces a large membrane shunt, reducing the efficacy of incoming EPSPs in driving the membrane potential towards the firing threshold. This decreases overall excitability, delaying AP onset without affecting AP threshold (20). In contrast, receptors located at the AIS, the site of AP initiation, are ideally positioned to directly influence the AP threshold. Rather than affecting the efficiency of EPSPs, they raise the AP threshold, thereby delaying AP onset (18, 20).

Taken together, these factors underscore the importance of understanding the subcellular localization of GlyRs, as it directly shapes how they modulate excitability. To fully understand their role in specific (patho)physiological contexts, and to effectively target them therapeutically, it is essential to elucidate their precise subcellular localization.

GlyRα2 as an important modulator of striatal signal integration - There are four GlyR α-subunits (α1–α4), each with distinct functional properties. Their expression patterns vary across brain regions and are developmentally regulated (24, 27). α2 is the predominant GlyR subunit expressed during development, with its expression declining sharply after birth (24, 28). Consequently, GlyRα2 has traditionally been studied in the context of neurodevelopment. However, recent evidence shows that functional GlyRα2 remains present in the adult dorsal striatum (29). Furthermore, it has been identified as the primary agonist-binding subunit expressed in both the adult dorsal and ventral striatum (29-31). This challenges the traditional view of GlyRα2 as merely a developmental subunit in the brain and highlights the adult striatum as a key site of GlyRα2 function.

The striatum is the main input site of the basal ganglia and a key component of the brain's reward circuitry. It integrates converging excitatory glutamatergic input from the cortex and thalamus, conveying sensory and motor information, with modulatory dopaminergic input from the midbrain, conveying motivational signals (32, 33). Here, dopamine functions as a gatekeeper ensuring that only motivationally relevant sensory and motor signals lead to striatal output (34). Dysregulation of striatal signal integration, caused by disruption of the E/I balance, distorts the processing of sensory and motor information, leading to abnormal striatal output and impaired reward-motivated behavior (33).

Recent evidence highlights GlyRα2 as an important modulator of striatal signal integration and striatum-related behavior (35). This positions GlyRα2 as a potential therapeutic target for restoring E/I balance and normalizing striatal output in disorders involving striatal dysfunction, such as psychosis, addiction and PD. The mechanisms through which it modulates striatal signal integration and thereby shapes striatal output remain largely unknown. As discussed above, the subcellular localization of GlyRs directly shapes how they modulate neuronal excitability. Therefore, elucidating the precise subcellular localization of GlyRα2 within striatal neurons is a critical step toward understanding how it modulates striatal signal integration.

mClYFP-GlyRα2: A Dual-Purpose Tool for Investigating GlyRα2 Localization and Activity - Previously, elucidating the subcellular localization of GlyRα2 was hindered by the lack of GlyRα2-specific antibodies. To overcome this limitation, our lab recently developed a novel chimeric fusion protein, mClYFP-GlyRα2. This innovative tool combines GlyRα2 with a yellow fluorescent protein-based Cl^--sensor (mClYFP) fused to its N-terminus, enabling high-resolution imaging of GlyRα2 localization at a subcellular level. Because the mClYFP tag functions as fluorescent chloride sensor, mClYFP-GlyRα2 also allows for real-time monitoring of receptor activity by detecting Cl^- flux through the channel.

When Cl^- binds in the protein's binding cavity, it stabilizes a protonated chromophore state that quenches fluorescence. Consequently, at high Cl^- concentrations, this quenching is strong and fluorescence intensity is reduced, while at lower Cl^- concentrations, quenching is weaker, resulting in increased fluorescence. Activation of GlyRα2 increases Cl^- conductance, altering local extracellular Cl^- levels and thereby producing measurable changes in mClYFP fluorescence. With enhanced sensitivity, photostability, and reduced pH sensitivity near physiological levels compared to other Cl^--sensors, mClYFP

effectively detects physiological changes in Cl^- concentration (Kd ~10 mM) (36). When fused to GlyRα2, it creates a powerful dual-purpose tool that enables simultaneous high-resolution, live-cell imaging of GlyRα2's subcellular localization and activity.

The primary goal of this study is to validate mClYFP-GlyRα2 as a reliable tool for investigating the subcellular localization and nanoscale activity of GlyRα2. To this end: (1) the conservation of ion channel properties in the chimeric protein is assessed using cell-attached single channel patch-clamp recordings; and (2) the sensitivity and functionality of the mClYFP sensor in response to glycine-induced receptor activation is evaluated using high-resolution live-cell imaging.

EXPERIMENTAL PROCEDURES

Cell culture – Human embryonic kidney 293 cells (HEK293 cells) were cultured in DMEM medium (41966-029, Gibco, UK) supplemented with 10% FBS (S181B-500, Biowest, South America) under standard conditions (37°C, 5% CO2). When cells reached 80-85% confluency, they were subcultured using trypsin/EDTA (25300-062, Gibco, UK) as detachment solution.

Calcium phosphate transfection - At least 24 hours before transfection, HEK293 were seeded in 35-mm diameter cultures dishes (627160, Greiner Bio-one, Germany). Seeded HEK293 cells were transfected with either a DNA plasmid encoding N-term tagged mClYFP-GlyRα2 or a DNA plasmid encoding the wild-type GlyRα2 via calcium phosphate co-precipitation. Transfection mixtures were prepared separately for each culture dish. A phosphate-DNA mix containing 86 µl 2x HEPES buffered saline (2xHBS) (280 mM NaCl, 10 mM KCl, 50 mM HEPES, 1.5 mM Na2HPO4.2H2O, 15 mM D-Glucose, pH7.1) and 200 ng plasmid DNA was made. To this mixture, 5.1 µl CaCl2 (2.5M) was added dropwise. After two minutes of incubation at RT, the mixture was added dropwise to the cells.

Cell-attached single-channel electrophysiology and analysis - Approximately 24 hours post-transfection, single-channel currents were recorded using the cell-attached configuration on HEK293 cells expressing either wild-type GlyRα2 or mClYFP-GlyRα2. Cells were visualized under an inverted Nikon microscope using a 40x objective. Patch pipettes, with a resistance of 6-11 MΩ, were pulled from filament-containing borosilicate glass capillaries (1403542, Hilgenberg, Germany) using a horizontal P-1000 micropipette puller (Sutter Instrument, USA). The external (bath) solution contained 150 mM NaCl, 2 mM KCl, 2 mM CaCl2, 1.2 mM MgCl2, 10 mM HEPES, 20 mM tetraethylammonium chloride (TEA-Cl), 15 mM Sucrose, and 14 mM glucose, adjusted to pH 7.4 with NaOH. Osmolality was measured using a freezing-point osmometer (Osmomat 030, Salmenkipp, The Netherlands). Patch pipettes were filled with triple filtered external solution supplemented with 30 µM glycine. Cell-attached recordings were performed in voltage-clamp mode at a holding potential of -60 mV using a HEKA EPC-10 amplifier (HEKA Elektronik, Germany) and PatchMaster software (HEKA Elektronik). Recordings were conducted at RT with a sampling rate of 50 kHz and a gain of 50 mV/pA, and filtered with a built-in 2.9 kHz low-pass filter. The liquid junction potential was considered 0 mV, and both the offset potential (V_0) and pipette capacitance (C_{fast}) were compensated prior to recording.

Analysis of the cell-attached single-channel recordings was performed using Clampfit 10.7 software (Molecular devices). Data acquired with HEKA PatchMaster was exported and converted into a compatible format using Excel prior to import into the Clampfit software. Recordings were digitally filtered with a 600 Hz low-pass Gaussian filter and a 50 Hz notch filter to reduce noise. The baseline current was manually adjusted to 0 pA. Single channel events were detected using Clampfit's 'Single Channel Search' function with a level contribution of 10% and a resolution threshold between 0-1 ms. All detected events were manually reviewed and either accepted or rejected to exclude false positives. Peak current amplitudes of the baseline and conductance levels, as well as single-channel conductance were determined using two complementary analysis approaches.

For the first method, data of multiple patches were pooled per construct (mClYFP-GlyRα2: n=9; WT GlyRα2: n=7). Amplitude histograms (Binwidth: 0.2 pA) were generated in Clampfit and fitted with multicomponential Gaussian functions using the Levenberg–Marquardt method with sum of squared errors minimization. This yielded best-fit peak current amplitudes for the baseline and main conductance levels. Unitary conductance was calculated as the current amplitude difference between the main

conductance and the baseline, divided by the holding potential (–60 mV):

$$\gamma\ (pS) = \frac{I_{Amp1}(pA) - I_{Amp0}\ (pA)}{-60\ mV}$$

For visualization, the histogram fits were re-plotted in GraphPad Prism 10.2.

For the second method, event lists for each individual patch were imported into Graphpad Prism, and amplitude histograms (binwidth: 0.2 pA) were generated. Current amplitudes falling outside the peak of the main conductance level were excluded. A double Gaussian function was fitted to each histogram to determine the best-fit amplitudes for the baseline and main conductance level. Unitary conductance was calculated for each patch as described above. Representative current time traces were exported from Clampfit (filtered and baseline adjusted) and imported into Graphpad Prism for figure generation.

High-resolution live-cell imaging and analysis - Raw live-cell imaging data of HEK293 cells transfected with mClYFP-GlyRα2 (n = 8) was kindly provided by Yana Vella. Briefly, HEK293 cells were seeded in 35-mm diameter glass-bottom culture dishes and transfected with 200 ng mClYFP-GlyRα2 DNA using calcium phosphate transfection. Twenty-four hours post-transfection, live-cell fluorescence imaging was performed using a Zeiss Elyra PS.1 widefield fluorescence microscope. Live-cell imaging data were acquired using Total Internal Reflection Fluorescence (TIRF) microscopy with an Alpha Plan-Apochromat 100x/1.46 Oil DIC M27 objective and a frame acquisition rate of 20 frames per second (fps). Cells were imaged in 25-second intervals during which a standardized five-phase stimulation protocol was applied (each phase lasting 5s): **[1]** 0s-5s: high extracellular Cl^- (160 mM), **[2]** 5s – 10s: low extracellular Cl^- (6 mM), **[3]** 10s - 15s: low Cl^- with glycine (10pM, 0.001µM, 0.1µM, 1µM and 100µM) or glycine (1µM) + strychnine (1µM), **[4]** 15s to 20s: low Cl^- washout, and **[5]** 20s to 25s: return to high Cl^- (160mM). The high Cl^- solution contained (in mM): 150 NaCl, 2 KCl, 2 $CaCl_2$, 1.2 $MgCl_2$, 10 HEPES, 20 TEA-Cl, 14 Glucose, 15 Sucrose; pH 7.4. The low Cl^- solution contained (in mM): 150 NaGluconate, 5.4 KGluconate, 2 $CaCl_2$, 1 $MgCl_2$, 10 HEPES, 10 Glucose; pH 7.4.

Live-cell imaging data were analysed using Microtome Image Analysis (MIA), a MATLAB-based software package. For each analysed cell (n=8), a single region of interest (ROI) encompassing the cell was manually defined and reused across all conditions. For each condition, raw image data were imported separately, and fluorescence intensity time traces were generated from the defined ROI. To correct for photobleaching, the uncorrected fluorescence intensity time trace was exported from MIA and fitted with a two-phase exponential decay function in GraphPad Prism. The fitted parameters were re-imported into MIA and applied to generate bleach-corrected traces.

To identify mClYFP-GlyRα2 positive pixels responsive to the shift from high to low extracellular Cl^-, a pixel-wise ratio image was computed for each condition by dividing the fluorescence intensity of each pixel during the final second of the low Cl^- time window (9–10 s) by that of the high Cl^- time window (4–5 s). Pixels with a ratio between 1.05 and 2.0 were considered responsive (threshold: 5%) and defined as mClYFP-GlyRα2 positive pixels. This ratio threshold was used to generate a new ROI containing only these Cl^--responsive pixels. Ratio images (heatmaps) visualizing the pixel-wise response were generated in MIA. Bleach-corrected fluorescence intensity time traces of the mClYFP-GlyRα2 positive pixel ROIs, as well as the number of positive pixels, were extracted and imported into GraphPad Prism and Excel for further analysis.

To identify pixels containing active GlyRα2 responsive to glycine application, a second ratio image was computed by dividing the fluorescence signal of each pixel during the final 2.5 seconds of the low Cl^- + glycine window (12.5–15 s) by that of the final second of the low Cl^- window (9–10 s). Pixels with a ratio between 0.8 and 0.95 were considered responsive (threshold: 5%) and defined as active GlyRα2 positive pixels. Corresponding ratio images (heatmaps) were generated, and the number of positive pixels was extracted and imported into GraphPad Prism and Excel for further analysis.

Bleach-corrected fluorescence intensity traces and pixel count data were analysed using GraphPad Prism and Microsoft Excel. For each condition and each cell (n=8), the mean fluorescence intensity was calculated from defined stimulus windows: 1.9–2.9 s (high Cl^-), 8.9–9.9 s (low Cl^-), and 12.45–14.9 s (glycine).

Fluorescence intensity values were normalized for visualization purposes as indicated in the figure legends. For high vs. low Cl^- comparisons, values were normalized to the high Cl^- condition; for low Cl^- vs. glycine comparisons, values were normalized to the low Cl^- condition.

Representative fluorescence intensity time traces were normalized to the mean of the low Cl^- time window to facilitate visual comparison.

Glycine-induced fluorescence changes were quantified as the percentage change relative to the low Cl^- baseline:

$$Fluorescence\ change\ (\%) = \frac{|F_{Gly} - F_{lowCl}|}{F_{lowCl}} * 100$$

where F_{Gly} and F_{lowCl} represent the mean fluorescence intensities during the glycine and low Cl^- time windows, respectively.

The percentage of GlyRα2 active pixels was calculated as the number of GlyRα2 positive pixels divided by the total number of mClYFP-GlyRα2 positive pixels for that condition.

Statistical analysis - All statistical analyses were performed using GraphPad Prism (v10.2). Data are presented as mean ± SEM. Outliers were identified using the ROUT method (Q = 1%). Data normality was assessed using the Shapiro–Wilk test. For comparisons between two experimental groups, either an unpaired t-test (single-channel recordings), a paired t-test (live-cell imaging), or a non-parametric Wilcoxon matched-pairs signed-rank test (live-cell imaging) was used, depending on the distribution and pairing of the data. Statistical significance was defined as $P < 0.05$.

RESULTS

The fusion of the protein-based chloride sensor (mClYFP) to the extracellular N-terminus of GlyRα2 could potentially influence ion channel properties, altering normal receptor function. Likewise, the fusion might interfere with the sensor's ability to accurately reflect Cl^--dependent fluorescence changes. Therefore, it is essential to validate that both the ion channel and Cl^--sensor retain their native functional and physiological properties in the chimeric protein before it can be reliably used to study GlyRα2's subcellular localization and nanoscale activity.

Conservation of ion channel properties in the chimeric protein – To assess whether GlyRα2 retains the intrinsic ion channel properties of native GlyRα2 in the chimeric protein, cell-attached single-channel patch clamp recordings were performed. Specifically, it was investigated whether fusion of the mClYFP sensor to the extracellular N-terminus of GlyRα2 alters the receptor's conductance, essential for its physiological function. HEK293 cells were transfected with either wild-type (WT) GlyRα2 or the chimeric mClYFP-GlyRα2 construct, enabling direct comparison of channel behavior under identical conditions. Clear single channel openings, activated by 30 µM Glycine, could be observed for both WT GlyRα2 and mClYFP-GlyRα2, as shown by the representative traces in figure 1A.

Two complementary analyses were performed to determine the current amplitude of the main (first) conductance level, representing single channel openings, from which unitary conductance was calculated.

First, amplitude histograms were generated by pooling events from all analyzed patches expressing mClYFP-GlyRα2 or WT GlyRα2 (n = 9 and n = 7, respectively). Gaussian fits were applied to identify the peak amplitudes of the baseline (closed state) and main (open state) conductance levels. This analysis yielded a peak amplitude of -2.77 ± 0.05 pA for mClYFP-GlyRα2 and -2.27 ± 0.02 pA for WT GlyRα2 for the main conductance level (Fig. 1B). Unitary conductance, calculated from the obtained peak amplitudes, was 45.4 pS for mClYFP-GlyRα2 and 38.4 pS for WT GlyRα2.

Second, amplitude histograms and Gaussian fits were generated for each individual patch, yielding peak amplitudes for nine mClYFP-GlyRα2 and seven WT GlyRα2 patches. The mean peak amplitude of the main conductance level was –2.58 ± 0.26 pA for mClYFP-GlyRα2 (n=9) and –2.24 ± 0.26 pA for WT GlyRα2 (n=7), with no significant difference between groups (t-test; p = 0.3635; Fig. 1C). Unitary conductance values, calculated from the obtained peak amplitudes per patch, ranged from 21.72 to 66.39 pS for mClYFP-GlyRα2 (mean 41.12 ± 4.08 pS) and from 19.25 to 58.13 pS for WT GlyRα2 (mean 35.59 ± 4.37 pS), again showing no significant difference between mClYFP-GlyRα2 and WT GlyRα2 (t-test, p = 0.3748; Fig. 1D).

These results demonstrate that fusion of mClYFP to GlyRα2 does not alter the receptor's unitary conductance, preserving its native single-channel current amplitude.

Although single-channel patch clamp recordings were performed, some patches likely contained multiple active channels. This occasionally resulted in simultaneous openings, which appeared as additional smaller peaks in the pooled amplitude histograms (Fig. 2A). These higher-amplitude peaks likely reflect the summation of multiple channels opening simultaneously, as indicated by their amplitudes being approximately integer multiples of the main

conductance level. Such events were observed in both mClYFP-GlyRα2 and WT GlyRα2 recordings and occurred with comparable frequency and amplitude (Fig. 2A).

In addition clear lower-amplitude events were observed in a small subset of patches from both mClYFP-GlyRα2 and WT GlyRα2. These single-channel openings had amplitudes between the baseline and main conductance level peak and generally exhibited a longer dwell time (Fig. 2B).

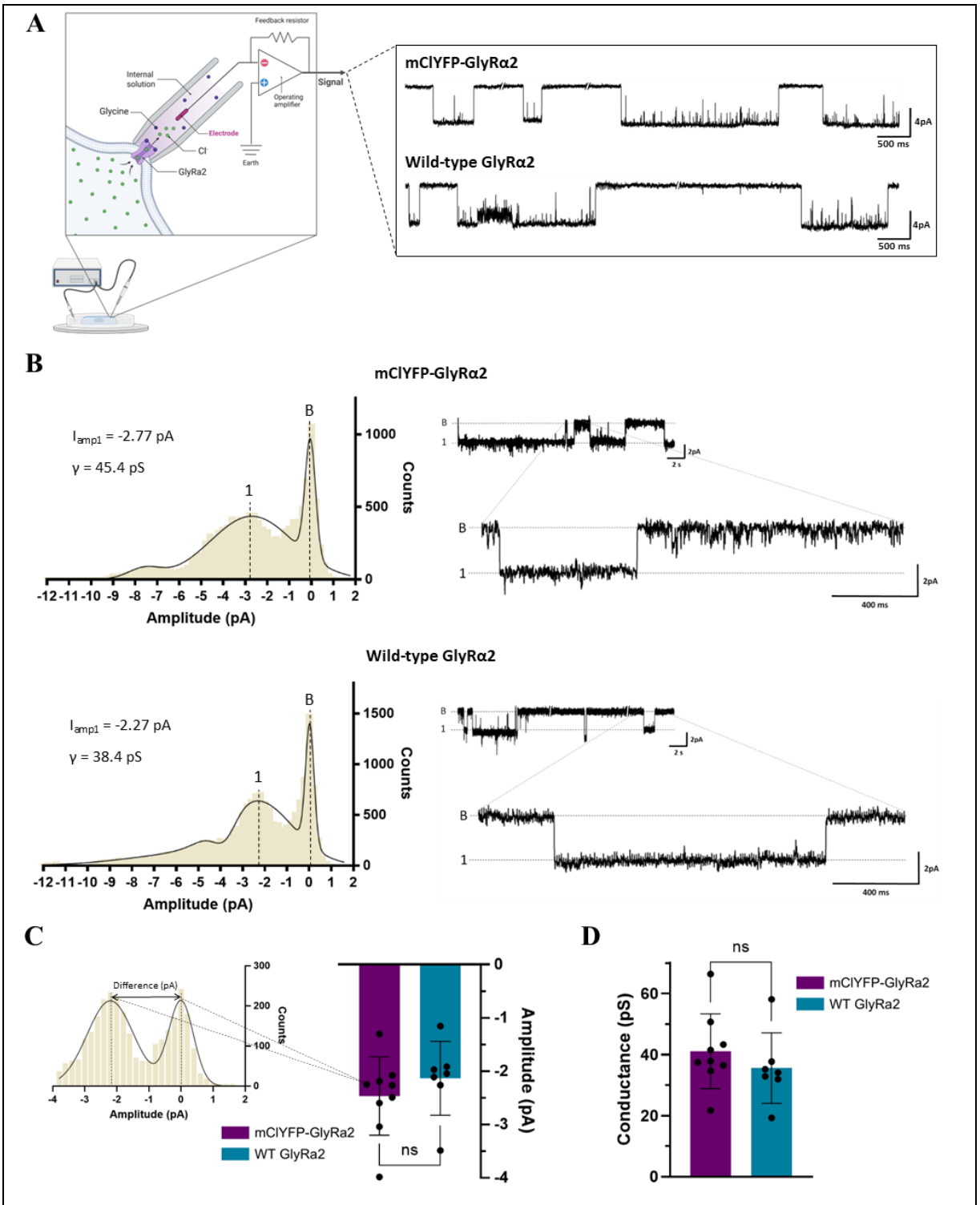

Fig. 1 – Single-channel current amplitude and unitary conductance of GlyRα2 are preserved in the chimeric protein (mClYFP- GlyRα2). To assess whether fusion of mClYFP to GlyRα2 affects its ion conduction properties, cell-attached single-channel patch-clamp recordings were performed on HEK293 cells transfected with either WT GlyRα2 or mClYFP-GlyRα2. **A)** Schematic representation of the experimental setup

(created with BioRender.com) and representative single-channel current time traces recorded at –60 mV from a WT GlyRα2 and mClYFP-GlyRα2 patch. Clear transitions between closed state and open state are visible in both constructs. **B)** Pooled all-point amplitude histograms of single-channel events (binwidth 0.2 pA) for mClYFP-GlyRα2 (n = 9 patches) and WT GlyRα2 (n = 7 patches), showing distribution of observed current amplitudes. The histograms were fitted with multi-Gaussian functions, yielding a best fit value for the peak current amplitudes of the baseline and main conductance level (I_{amp1}), from which unitary conductances (γ) were calculated. Corresponding representative traces recorded at -60mV are shown with the baseline (B) and main conductance level (1) annotated. **C)** Example of an individual amplitude histogram from a single patch (binwidth 0.2 pA), illustrating how the peak current amplitude was determined. A double Gaussian fit was applied to identify peak current amplitudes for the baseline and main conductance level. The difference between these peaks was calculated as the single-channel current amplitude for that patch. This difference (pA) is indicated on the histogram by an arrow and corresponds to one datapoint in the adjacent bar graph. The bar graph compares mean single-channel current amplitudes between mClYFP-GlyRα2 (n = 9) and WT GlyRα2 (n = 7), showing no significant difference (mClYFP-GlyRα2: –2.58 ± 0.26 pA; WT: –2.24 ± 0.26 pA). **D)** Bar graph showing the mean unitary conductance for mClYFP-GlyRα2 (n = 9) and WT GlyRα2 (n = 7), calculated for each patch as the single-channel current amplitude divided by the holding potential (-60 mV). No significant difference was observed between groups (mClYFP-GlyRα2: 41.12 ± 4.08 pS; WT: 35.59 ± 4.37 pS). Quantitative data are presented as mean ± SEM from 9 (mClYFP-GlyRα2) or 7 (WT GlyRα2) independent recordings. Statistical significance was assessed using unpaired t-tests; outliers were evaluated with a ROUT test (Q = 1%), and data normality was confirmed using the Shapiro–Wilk test.

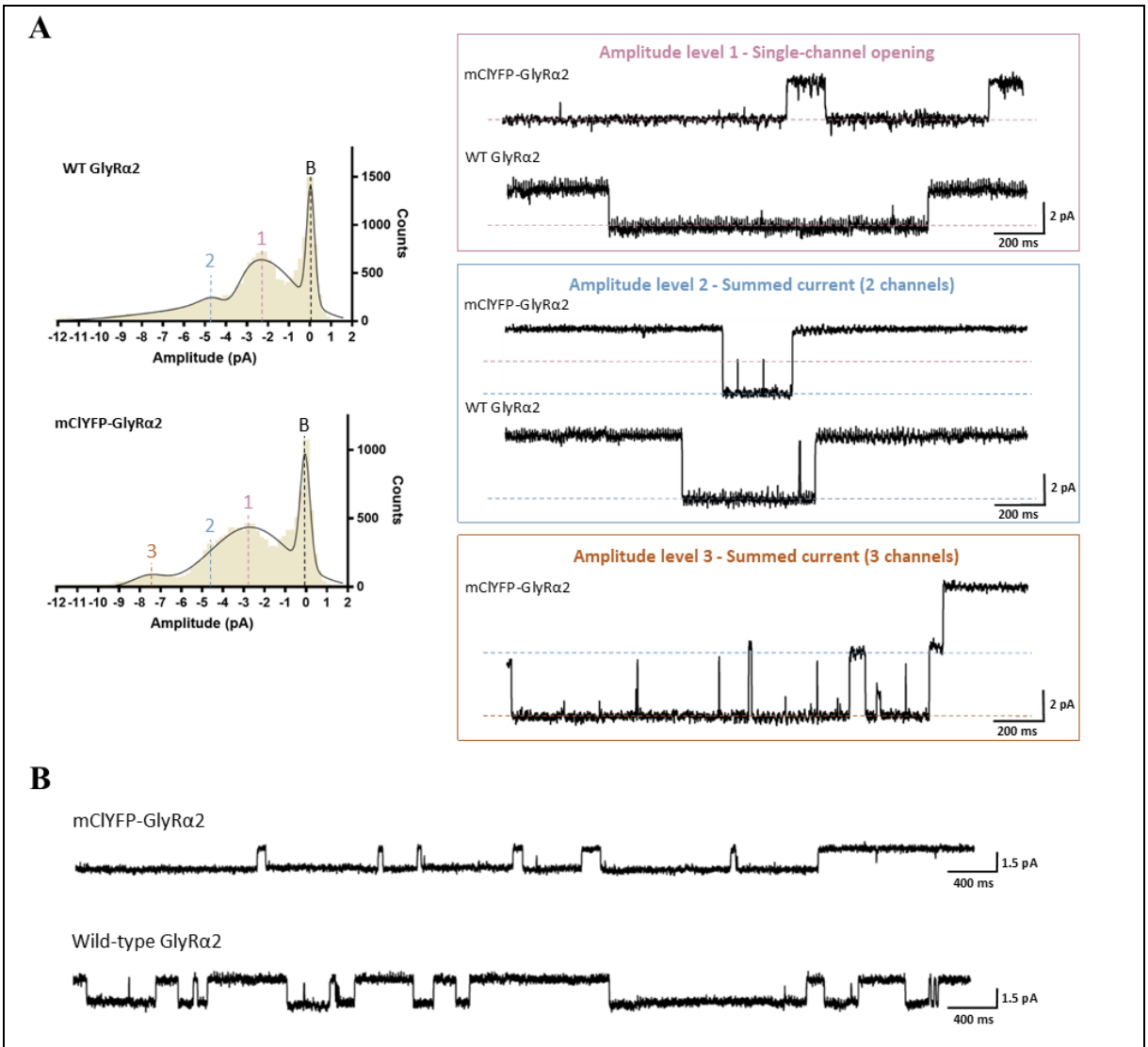

Fig. 2 – Multiple current amplitude levels and lower-amplitude openings were observed in single-channel recordings of WT GlyRα2 and mClYFP-GlyRα2. A) Pooled all-point amplitude histograms of single-channel

events (binwidth 0.2 pA) from WT GlyRα2 (n = 7 patches) and mClYFP-GlyRα2 (n = 9 patches), showing multiple distinct amplitude peaks. In addition to the main peak corresponding to the main conductance level (amplitude level 1), additional smaller peaks were observed at approximately integer multiples of amplitude level 1 (levels 2 and 3), consistent with simultaneous openings of multiple channels within the same patch. Vertical lines indicate the location of each amplitude peak. Representative single-channel traces recorded at –60 mV are shown for amplitude levels 1, 2, and 3 for both constructs, color-coded to match the corresponding peaks in the histograms. **B)** Representative single-channel traces recorded at –60 mV from WT GlyRα2 and mClYFP-GlyRα2 patches, showing distinct lower-amplitude events with amplitudes between the baseline and amplitude level 1 peak (1-2 pA). These events were observed in a subset of patches from both constructs and generally exhibited a longer dwell time.

Functionality and sensitivity of the mClYFP sensor in the chimeric protein – To assess whether the mClYFP chloride sensor retains its Cl^--sensing properties when fused to GlyRα2, and to validate the functionality and sensitivity of the mClYFP-GlyRα2 fusion protein as a reporter of GlyRα2 activity, high-resolution live-cell fluorescence imaging was performed in HEK293 cells transiently transfected with mClYFP-GlyRα2. Cells were sequentially exposed to controlled extracellular Cl^- and glycine conditions to manipulate Cl^- gradients and induce receptor activation. mClYFP fluorescence intensity was measured over time using TIRF microscopy, which enables selective imaging of membrane-proximal signals, ideal for this membrane-embedded receptor. A standardized five-phase stimulation protocol was applied during imaging (Fig. 3A).

First, the functionality of the mClYFP sensor in the fusion protein was assessed by monitoring changes in fluorescence intensity in response to a change from high to low extracellular Cl- levels. For all analyzed cells (n = 8), the mean fluorescence intensity was calculated over defined time windows corresponding to the high and subsequent low chloride conditions. The results revealed a significant difference in mean fluorescence intensity between conditions (Wilcoxon matched-pairs signed rank test, p = 0.0078, n = 8), with an increase of 13.19% under low Cl^- (Fig. 3B). This demonstrates that the mClYFP sensor produces a fast and measurable response to changes in extracellular Cl^-, confirming that it retains its Cl^--sensing properties when fused to GlyRα2.

Next, to assess whether the mClYFP-GlyRα2 fusion protein can report glycine-induced Cl^- flux through GlyRα2 and thus function as a reporter of receptor activity, changes in fluorescence intensity in response to glycine application were analyzed. The mean fluorescence intensity during the defined low Cl^- time window was compared to that during glycine application, when GlyRα2 channels are expected to open and allow Cl^- efflux (due to the low extracellular Cl^- environment). The results revealed a significant difference in mean fluorescence intensity between conditions (Paired t-test, p = 0.0006, n = 8), with an average decrease of 3.25% upon glycine application (Fig. 3C). This demonstrates that glycine-induced GlyRα2 activation produces a robust and measurable change in mClYFP fluorescence intensity, confirming mClYFP-GlyRα2's functionality as a real-time reporter of GlyRα2 activity.

When strychnine, a competitive GlyR antagonist, was co-applied with glycine, the glycine-induced change in fluorescence intensity was significantly reduced compared to glycine alone (1.66% vs. 3.19%; Wilcoxon matched-pairs signed rank test, p = 0.0078; Fig. 3D and E). Complementing this, the percentage of pixels showing glycine-induced changes in fluorescence intensity, representing pixels where GlyRα2 is active, was also significantly lower in the presence of strychnine (15.82% vs. 28.08%; Wilcoxon matched-pairs signed rank test, p = 0.0078; Fig. 3F). These findings show that glycine-induced fluorescence quenching is blocked by strychnine, confirming that the observed change is mediated by GlyRα2 activation. This supports the specificity and functionality of the mClYFP-GlyRα2 fusion protein as a reporter of GlyRα2 activity.

To identify regions of mClYFP-GlyRα2 expression and map GlyRα2 activity at nanoscale resolution, pixel-wise fluorescence ratio images were generated. First, to identify pixels within the ROI where the chimeric protein is expressed, a ratio was calculated between the final second of the high Cl^- condition (4–5 s) and the final second of the low Cl^- condition (9–10 s). Pixels with a fluorescence ratio >1.05 (i.e., showing an increase in fluorescence intensity >5% in response to the Cl^- shift) were identified as mClYFP-GlyRα2 expressing pixels. To detect GlyRα2 activity upon glycine application, a second ratio was calculated

between the final 2.5 seconds of glycine application (12.5–15 s) and the final second of the low Cl^- condition (9–10 s). Pixels with a fluorescence ratio <0.95 (i.e., showing a fluorescence decrease >5% in response to glycine) were identified as GlyRα2-active at that moment. These ratio calculations are used to generate heatmaps showing GlyRα2 activity at a given timepoint with high spatial resolution (Fig. 3G). This pixel-based analysis demonstrates the unique potential of live-cell TIRF imaging of mClYFP-GlyRα2–transfected cells to visualize GlyRα2 activity with nanoscale resolution.

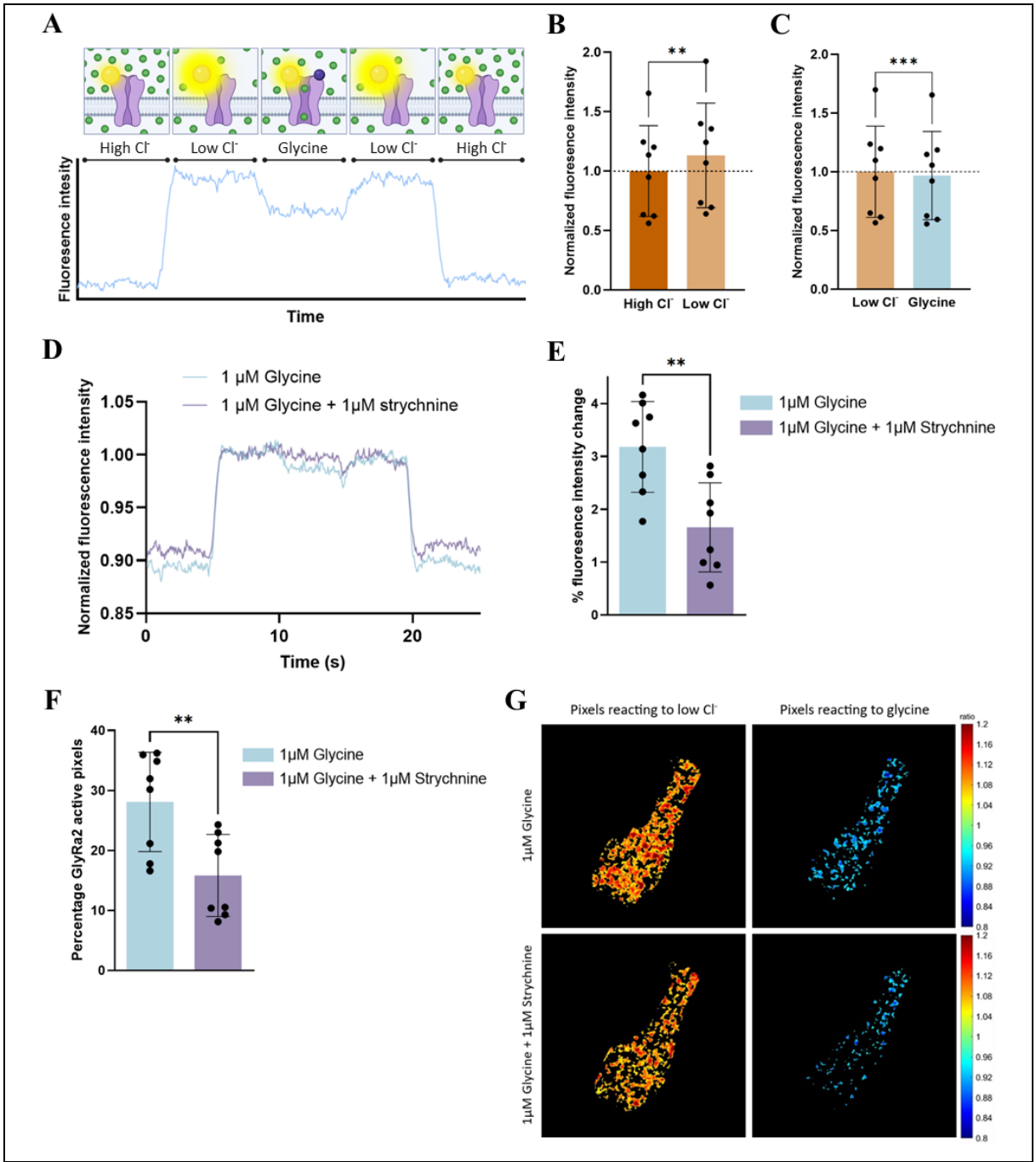

Fig. 3 – mClYFP-GlyRα2 retains Cl^- sensitivity and reports glycine-induced receptor activation. To determine whether the mClYFP chloride sensor remains functional when fused to GlyRα2, and whether the fusion construct can report glycine-induced GlyRα2 activity, HEK293 cells expressing mClYFP-GlyRα2 were imaged using live-cell TIRF microscopy during a five-phase stimulation protocol. **A)** Schematic representation of the five sequential extracellular conditions applied during imaging (each lasting 5 seconds): (1) high Cl^- (160 mM) (baseline), (2) low Cl^- (6 mM) (to establish a Cl^- gradient), (3) low Cl^- + glycine (to activate GlyRα2 and induce Cl^- flux), (4) low Cl^- washout, and (5) return to high Cl^-. Example of a resulting fluorescence intensity time trace is shown, with illustrations of mClYFP-GlyRα2 behavior at each phase (created with BioRender.com).

B) Bar graph comparing mean mClYFP fluorescence intensity during defined high Cl^- (1.9–2.9 s) and low Cl^- (8.9–9.9 s) time windows in 8 individual cells. Data were normalized to the high Cl^- condition for visualization. A significant increase in fluorescence intensity was observed upon Cl^- reduction (13.19% increase). **C)** Bar graph comparing mean mClYFP fluorescence intensity during defined low Cl^- (8.9–9.9 s) and low Cl^- + glycine (12.45–14.9 s) time windows (n=8). Data were normalized to the low Cl^- condition for visualization. A significant decrease in fluorescence intensity was detected upon glycine application (3.25% decrease). **D)** Representative bleach-corrected fluorescence intensity time traces from one cell when exposed to either 1 µM glycine alone or 1 µM glycine + 1 µM strychnine. Data were normalized to the mean intensity of the corresponding low Cl^- window (6.0–9.9 s and 16.0–19.1 s) for direct visual comparison of the change in fluorescence intensity upon glycine application between conditions. **E)** Bar graph showing percentage change in fluorescence intensity between low Cl^- (8.9–9.9 s) and glycine (12.45–14.9 s) conditions for 1 µM glycine alone and with 1µM strychnine co-application (n=8). The glycine-induced fluorescence decrease was significantly reduced in the presence of strychnine (3.25% vs. 1.66%). **F)** Bar graph comparing the percentage of active GlyRα2-positive pixels (i.e., pixels showing glycine-induced responses) between 1µM glycine alone and with 1µM strychnine co-application (n=8). Significantly fewer responsive pixels were observed with strychnine (28.08% vs. 15.82%). **G)** Representative ratio images (heatmaps) showing pixel-wise responses from a single cell for 1µM Glycine and 1µM glycine + 1µM strychnine. The left panels show Cl^--responsive mClYFP-GlyRα2-positive pixels (ratio: low Cl^- / high Cl^-), and the right panels show glycine-responsive (active GlyRα2) pixels (ratio: glycine / low Cl^-). Responsive pixels were identified using a 5% change threshold (see Methods). Color scales reflect the fluorescence ratio at each pixel. Quantitative data are presented as mean ± SEM. Statistical significance was assessed using paired t-tests or Wilcoxon matched-pairs signed-rank tests as appropriate. outliers were evaluated with a ROUT test (Q = 1%), and data normality was confirmed using the Shapiro–Wilk test. **P<0.01, ***P<0.001

To further evaluate the sensitivity and dynamic range of the mClYFP-GlyRα2 reporter, changes in fluorescence intensity upon glycine application were assessed across a range of concentrations (10 pM to 100 µM). Representative time traces show detectable glycine-induced fluorescence quenching at concentrations as low as 1 nM, with maximal responses at 0.1 µM and a decline at the highest concentration tested (100 µM) (Fig. 4B). Quantification of the fluorescence changes showed decreases of 1.50%, 3.65%, 4.45%, 3.18%, and 2.53% for 10 pM, 1 nM, 0.1 µM, 1 µM, and 100 µM glycine, respectively (Fig. 4A).
To further quantify GlyRα2 activation across glycine concentrations, the percentage of pixels exhibiting glycine-induced changes in fluorescence intensity, indicative of active GlyRα2, was quantified for each concentration. This pixel-based readout followed a similar trend to the whole-cell fluorescence intensity changes. The percentage of glycine-responsive pixels increased with concentration up to 0.1 µM (10 pM: 18.20%, 1 nM: 31.71%, 0.1 µM: 37.59%), followed by a moderate decline at higher concentrations (1 µM: 28.08%, 100 µM: 25.92%) (Fig. 4C).
Together, these results demonstrate that mClYFP-GlyRα2 can detect glycine-induced chloride flux and report GlyRα2 activity across a broad concentration range, including very low (sub-nanomolar) levels. This supports its sensitivity and effectiveness as a real-time reporter of GlyRα2 activation.

DISCUSSION

Disruption of E/I balance in the CNS is a hallmark of various psychiatric and neurological disorders, including autism, psychosis, dementia, and PD (1-4). The imbalance leads to abnormal information processing, contributing to the characteristic symptoms of these conditions. GlyRs, which are essential for maintaining E/I balance in the CNS, have been suggested as promising therapeutic targets for reestablishing this balance, and thereby normalizing information processing (5-8). However, their modulatory effects are highly context-dependent, shaped by their cell type-specific subcellular localization and activity (18, 20). To understand their function in specific (patho)physiological contexts and to inform the development of effective targeted therapies, it is therefore essential to elucidate their localization and activity at a subcellular level. Progress in this area has long been limited by the lack of suitable tools.

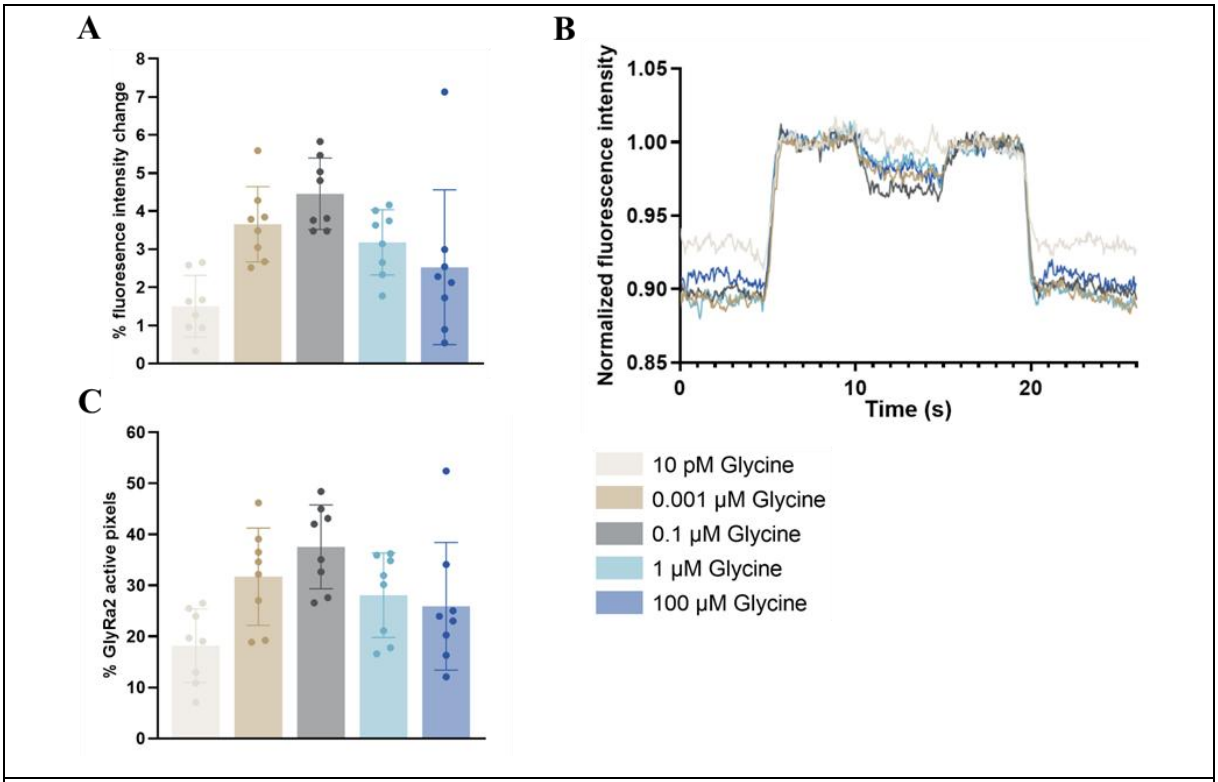

Fig. 4 – mClYFP-GlyRα2 detects glycine-induced receptor activation across a broad concentration range. To assess the sensitivity and dynamic range of the mClYFP-GlyRα2 reporter, HEK293 cells expressing mClYFP-GlyRα2 were exposed to increasing concentrations of glycine (10 pM to 100 µM) under low Cl^- conditions, and fluorescence responses were monitored using live-cell TIRF microscopy. **A)** Bar graph showing the percentage change in mClYFP fluorescence intensity between defined low Cl^- (8.9–9.9 s) and glycine (12.45–14.9 s) time windows for each glycine concentration (n=8). Maximal quenching was observed at 0.1 µM glycine, with a decline in fluorescence change at 1 µM and 100 µM. **B)** Representative bleach-corrected fluorescence intensity time traces from one cell exposed to each glycine concentration. Data were normalized to the mean intensity of the corresponding low Cl^- time window (6.0–9.9 s and 16.0–19.1 s) for direct visual comparison of the change in fluorescence intensity upon glycine application between conditions. **C)** Bar graph showing the percentage of glycine-responsive (active GlyRα2-positive) pixels at each glycine concentration (n=8). The proportion of responsive pixels increased with glycine concentration up to 0.1 µM, followed by a decrease at higher concentrations. Quantitative data are presented as mean ± SEM.

In this study, a novel chimeric fluorescent reporter, mClYFP-GlyRα2, designed to simultaneously assess the subcellular localization and activity of GlyRα2, was presented and validated. The findings demonstrate that fusion of the Cl^--sensitive fluorescent protein mClYFP to the extracellular N-terminus of GlyRα2 (1) does not alter the receptor's native unitary conductance, (2) preserves the Cl^--sensing functionality of the mClYFP sensor, and (3) enables real-time fluorescence-based detection of receptor activation. These findings were supported by single-channel patch clamp recordings, which showed no significant difference in main conductance level amplitude or unitary conductance between mClYFP-GlyRα2 and wild-type GlyRα2. In addition, live-cell TIRF imaging revealed a significant change in mClYFP fluorescence intensity in response to changes in extracellular Cl^-, as well as significant glycine-induced fluorescence quenching that was blocked by strychnine. Together, these findings, supported by previously obtained whole-cell electrophysiology data confirming GlyRα2 activity, validate mClYFP-GlyRα2 as a reliable tool for nanoscale activity mapping GlyRα2.

GlyRα2 is a pentameric, ligand-gated Cl^- channel that modulates neuronal excitability by regulating the flow of Cl^- ions across the neuronal membrane. Proper conduction of Cl^- through open GlyRα2 channels is essential for normal receptor function. Functional GlyRα2 receptors are typically composed of five agonist-binding α2-subunits, or four α2-subunits and one structural β-subunit. Each subunit contains a long extracellular N-terminus, to which mClYFP is

fused in the chimeric reporter construct. This substantial structural modification raised the possibility that the added mClYFP sensors might hinder formation of functional channels or interfere with its ion conduction properties. This could cause disruption of highly regulated neuronal networks, compromising E/I balance and network activity, which could, in turn, compromise interpretation of GlyRα2's function in the studied (patho)physiological context.

To address this, in this study cell-attached single-channel patch clamp recordings were performed under identical conditions for both mClYFP-GlyRα2 and WT GlyRα2. These measurements were used to determine whether the chimeric receptor retained its native unitary conductance, that is, the current amplitude associated with the opening of a single channel pore, which is a primary requirement for the validity of mClYFP-GlyRα2.

Clear single channel openings were observed for both WT GlyRα2 and mClYFP-GlyRα2 in transfected HEK293 cells (Fig. 1A). HEK293 cells are widely used model system for studying GlyRs. They do not express GlyRs endogenously, ensuring that all recorded channel activity originated from the transfected constructs (37). These observations confirm that the chimeric mClYFP-GlyRα2 construct is capable of forming functional ion channels. Single-channel recordings further showed that the unitary conductance of mClYFP-GlyRα2 was comparable to that of WT GlyRα2. While pooled amplitude histograms suggested a slightly higher peak current amplitude and calculated unitary conductance for the chimeric receptor, statistical analysis of individual patch recordings revealed no significant difference in peak current amplitude or unitary conductance between the two groups. These results indicate that fusion of mClYFP to the extracellular N-terminus of GlyRα2 does not hinder formation of functional ion channels and does not significantly interfere with its ion conduction properties. This is a key validation step, demonstrating that mClYFP-GlyRα2 can be reliably used to study GlyRα2 at a subcellular level in complex neuronal networks.

The peak current amplitudes observed in this study for both WT GlyRα2 (-2.27 pA) and mClYFP-GlyRα2 (-2.77 pA) were noticeably lower than those reported for WT GlyRα2 in previous studies (38-41). This discrepancy is likely attributable to differences in recording configurations and holding potentials, which affect the driving force of Cl^- ions and consequently influence current amplitude. For example, Bormann *et al.*, who reported peak amplitudes between -3 and -5 pA, used outside-out recordings, allowing control over both intra- and extracellular Cl^- concentrations, and applied a holding potential of -70 mV (38). Krashia *et al.* conducted cell-attached recordings, but at a markedly depolarized holding potential of +100 mV, observing peak amplitudes of around 6 pA (39). Amplitudes more similar to those observed in this study were reported by Zhang *et al.* (-3.2 pA) and Yu *et al.* (-3.8 pA), who used outside-out recordings with holding potentials of -70 mV and -50 mV, respectively (40, 41). In contrast, the present study employed cell-attached recordings at –60 mV, where only the extracellular Cl^- concentration could be controlled. These distinct experimental conditions likely resulted in a reduced driving force for Cl^-, and thus smaller recorded amplitudes. Importantly, however, the aim of this experiment was not to compare mClYFP-GlyRα2 amplitudes to values obtained in previous studies, but rather to those of WT GlyRα2 under identical experimental conditions in order to assess whether fusion of mClYFP affects ion conduction. From this perspective, the absence of a significant difference in peak current amplitude and unitary conductance supports the conclusion that the fusion does not impair the channel's fundamental conductive properties.

A possible limitation of the present approach is the use of the cell-attached configuration, which prevents precise control or measurement of intracellular chloride concentration. As a result, the driving force for Cl^- cannot be accurately determined, and calculated unitary conductance values should be interpreted as approximate. However, because both mClYFP-GlyRα2 and WT GlyRα2 were recorded and analyzed under identical conditions, this limitation does not compromise the validity of the comparative analysis, which remains the primary focus of this study.

In addition to the main conductance level, distinct lower-amplitude events were observed in a small subset of patches from both WT GlyRα2 and mClYFP-GlyRα2 (Fig. 2B). These events exhibited clear, rapid onset and offset transitions characteristic of single-channel openings, and were therefore unlikely to be recording artifacts. However, their amplitudes ranged from –1 to –1.5 pA and their dwell times were generally longer than those of full-amplitude openings. One possible explanation is that these represent

subconductance states of GlyRα2, which have been described in other ligand-gated ion channels (42, 43). However, unlike typical subconductance events, which tend to occur transiently and interspersed with full openings, these events sometimes constituted the predominant or sole activity within a given patch.

This observation raises the alternative possibility that the events reflect activity of endogenous low-conductance ion channels present in HEK293 cells. Although endogenous channel activity in native HEK293 cells was traditionally considered negligible, increasing numbers of ion channels have been identified in this model system (44). For example, HEK293 cells endogenously express Piezo1 channels, which can be activated by mechanical stimuli such as negative pressure applied through the patch pipette. In a recent study, Piezo1-mediated currents recorded in cell-attached patches at -60 mV in response to –30 mmHg of negative pressure exhibited a main open-state amplitude of -1.5 pA, along with multiple subconductance levels at -0.5 and -1.1 pA (45). Given that the present recordings were also performed in cell-attached mode at –60 mV, and that comparable negative pressure was likely applied by mouth during patching, it is plausible that the observed events reflect endogenous Piezo1 activity.

Alternatively, HEK293 cells also express calcium-activated chloride channels (CaCCs), which have been shown to generate low-amplitude openings at negative membrane potentials upon local increases of intracellular calcium (46). As the pipette and bath solutions in this study contained 2.5 mM $CaCl_2$, localized calcium influx cannot be excluded and may have contributed to sporadic activation of endogenous CaCCs.

While the exact origin of the low-amplitude events cannot be definitively determined in the present study, their presence in both WT and chimeric recordings under identical conditions, with similar frequency and properties, suggests that they are unrelated to the mClYFP fusion and do not compromise the conclusion that mClYFP-GlyRα2 retains normal ion conduction properties under the experimental conditions tested.

mClYFP is a yellow fluorescent protein-based Cl^--sensor originally developed by Zong *et al.* (36). With its enhanced Cl^- sensitivity, photostability, and reduced pH sensitivity near physiological levels compared to other Cl^--sensors, it is ideally suited to detect subtle, local changes in Cl^- concentration that occur upon the opening of individual GlyRα2 channels. Binding of $Cl^–$ ions to the sensor's binding cavity leads to fluorescence quenching; thus, fluctuations in local $Cl^–$ levels can be detected as measurable changes in fluorescence intensity using high-resolution live-cell imaging. These properties made mClYFP a excellent candidate for incorporation into the chimeric fluorescent reporter, mClYFP-GlyRα2, designed for nanoscale activity mapping of GlyRα2 in living cells.

However, fusion of mClYFP to the extracellular N-terminus of GlyRα2 could potentially alter the sensor's structural integrity, thereby compromising its functionality. To validate that mClYFP retained its ability to report changes in Cl^- concentration by changes in fluorescence intensity when fused to GlyRα2, fluorescence intensity changes were assessed in mClYFP-GlyRα2-expressing HEK cells during a controlled shift from high to low extracellular $Cl^–$ using live-cell TIRF imaging. The results showed a significant and rapid increase in fluorescence intensity in response to $Cl^–$ reduction, confirming that the mClYFP sensor retains its functionality in the chimeric protein, producing a significant fluorescence response to changes in extracellular Cl^-. Notably, the fluorescence change occurred almost immediately following the change in $Cl^–$ levels, demonstrating that the sensor responds with high temporal precision. This surprisingly fast reaction underscores the sensor's sensitivity, providing near real-time feedback on changes in local $Cl^–$ levels.

Having confirmed that mClYFP retains its Cl^- sensing functionality in the chimeric construct, the next step was to determine whether mClYFP-GlyRα2 can reliably detect subtle, local changes in $Cl^–$ levels resulting from GlyRα2 activation, and thereby report glycine-induced receptor activity in real time. When glycine was applied in a low extracellular Cl^- environment, favoring Cl^- efflux, a rapid and significant decrease in fluorescence intensity of mClYFP was observed, consistent with increased local $Cl^–$ levels due to GlyRα2 channel opening. This confirms that mClYFP-GlyRα2 can report receptor activity by producing a measurable change in fluorescence intensity in response to small local changes in extracellular Cl^- associated with receptor activation and supports its use for nanoscale activity mapping of GlyRα2. Co-application of glycine with strychnine, a GlyR antagonist, confirmed that the observed change in fluorescence intensity upon glycine application was indeed caused by receptor activation, further

strengthening the conclusion that mClYFP-GlyRα2 can accurately report GlyRα2 activity.

The ability of mClYFP-GlyRα2 to detect fluorescence changes at glycine concentrations as low as 1 nM highlights the high sensitivity of the reporter. This is especially valuable in physiological contexts, where extracellular glycine levels are typically low. The enhanced sensitivity is likely attributable not only to the intrinsic properties of mClYFP but also to the fact that each functional GlyRα2 receptor carries four or five copies of the sensor on its extracellular surface, amplifying local signal detection.

At higher glycine concentrations, a lower change in fluorescence intensity was observed. This is likely due to the absence of voltage control in the unpatched setup, where the driving force for Cl^- efflux may be diminished, leading to reduced net Cl^- flux and consequently a smaller fluorescence response. In whole-cell patch-clamp experiments using the same construct, increased pixel activity and fluorescence changes are still observed at high glycine concentrations (data not shown). The pixel-based analysis supports this, showing a reduced number of pixels containing active GlyRα2 at the highest glycine concentrations. These findings reinforce the physiological relevance of the mClYFP-GlyRα2 reporter, demonstrating its ability to detect GlyRα2 activation across a broad range of glycine concentrations, and revealing response patterns consistent with receptor desensitization at high agonist levels.

In this study, imaging data from mClYFP-GlyRα2-transfected HEK cells were analyzed using a pixel-based method for nanoscale activity mapping implemented in PAM, a MATLAB-based software developed by Schrimpf *et al.* (47). This approach enables not only the quantification of overall fluorescence intensity changes, but also the identification of individual pixels that exhibit Cl^-- or glycine-induced fluorescence responses, thereby providing subcellular resolution of receptor localization and activity. Pixels that respond to a shift from high to low extracellular Cl^- identify regions containing mClYFP-GlyRα2, while pixels that respond to glycine application represent active GlyRα2 at that given timepoint. In future applications, this method could be extended to neuronal systems to investigate the subcellular distribution of GlyRα2, by quantifying responsive pixels in dendrites, soma, and axons, and to explore how GlyRα2's nanoscale activity patterns vary in response to synaptic stimulation in defined neuronal circuits. Such capabilities would provide valuable insight into the spatial organization and activity of GlyRα2 in physiologically relevant contexts.

CONCLUSION

In summary, this study validates the novel chimeric fluorescent reporter, mClYFP-GlyRα2, as a reliable tool for nanoscale activity mapping of GlyRα2. The results demonstrate that fusion of the Cl^--sensitive fluorescent protein mClYFP to the extracellular N-terminus of GlyRα2 does not alter the receptor's native unitary conductance, confirming conservation of ion channel properties. Furthermore, they show that mClYFP retains its Cl^--sensing functionality in the chimeric protein and enables real-time fluorescence-based detection of glycine-induced receptor activation, demonstrating the sensitivity and functionality of the sensor. Together, these findings support the use of mClYFP-GlyRα2 for studying the subcellular localization and activity of GlyRα2 in complex physiological contexts with high spatial and temporal resolution.

Applying this tool in the adult striatum will help gain a deeper understanding of how GlyRα2 modulates striatal signal integration, potentially guiding the development of targeted therapies aimed at restoring E/I balance in disorders involving striatal dysfunction, such as psychosis, addiction and PD.

While originally developed to study GlyRα2 in the striatum, this tool is broadly applicable to other (patho)physiological contexts where GlyRα2 is involved. Moreover, it could serve as a screening platform for pharmacological compounds, aiding the development of GlyRα2-targeted therapeutics.

Finally, since GlyRs belong to the Cys-loop receptor family, which includes other receptors critical for E/I regulation, such as GABAA receptors and nicotinic acetylcholine receptors, and is characterized by conserved structural architecture across receptors, mClYFP-GlyRα2 may serve as a blueprint for designing analogous activity reporters. Such tools would enable investigations into the subcellular localization and functional dynamics of other Cys-loop receptors, with potential therapeutic relevance across a broad range of CNS disorders involving disrupted E/I balance.

REFERENCES

1. Metkus JD, Blanco T, Mohan A, Oh A, Robinson C, Bhattacharya S. Chapter 27 - Excitation–inhibition balance in diseases of the brain: Role of NMDA and GABA receptors. In: Bagchi D, Chaurasia RN, Ohia SE, editors. A Review on Diverse Neurological Disorders: Academic Press; 2024. p. 353-83.
2. He HY, Cline HT. What Is Excitation/Inhibition and How Is It Regulated? A Case of the Elephant and the Wisemen. J Exp Neurosci. 2019;13:1179069519859371.
3. Bruining H, Hardstone R, Juarez-Martinez EL, Sprengers J, Avramiea AE, Simpraga S, et al. Measurement of excitation-inhibition ratio in autism spectrum disorder using critical brain dynamics. Sci Rep. 2020;10(1):9195.
4. Bhatia A, Moza S, Bhalla US. Precise excitation-inhibition balance controls gain and timing in the hippocampus. Elife. 2019;8.
5. Kasaragod VB, Schindelin H. Structure-Function Relationships of Glycine and GABA(A) Receptors and Their Interplay With the Scaffolding Protein Gephyrin. Front Mol Neurosci. 2018;11:317.
6. Maric HM, Kasaragod VB, Hausrat TJ, Kneussel M, Tretter V, Strømgaard K, et al. Molecular basis of the alternative recruitment of GABA(A) versus glycine receptors through gephyrin. Nat Commun. 2014;5:5767.
7. Maynard S, Schulte C, Laurent F, Masson J-B, Maric H, Gosse C, et al. Competition between glycine and GABAA receptors for gephyrin controls their equilibrium populations at inhibitory synapses2024.
8. Trombley PQ, Hill BJ, Horning MS. Interactions between GABA and glycine at inhibitory amino acid receptors on rat olfactory bulb neurons. J Neurophysiol. 1999;82(6):3417-22.
9. Nys M, Kesters D, Ulens C. Structural insights into Cys-loop receptor function and ligand recognition. Biochem Pharmacol. 2013;86(8):1042-53.
10. Tsetlin V, Kuzmin D, Kasheverov I. Assembly of nicotinic and other Cys-loop receptors. Journal of Neurochemistry. 2011;116(5):734-41.
11. Le-Corronc H, Rigo JM, Branchereau P, Legendre P. GABA(A) receptor and glycine receptor activation by paracrine/autocrine release of endogenous agonists: more than a simple communication pathway. Mol Neurobiol. 2011;44(1):28-52.
12. Burgos CF, Yevenes GE, Aguayo LG. Structure and Pharmacologic Modulation of Inhibitory Glycine Receptors. Mol Pharmacol. 2016;90(3):318-25.
13. Lynch JW. Molecular structure and function of the glycine receptor chloride channel. Physiol Rev. 2004;84(4):1051-95.
14. Tang Z-Q, Lu Y-G, Huang Y-N, Chen L. Cross-talk pattern between GABAA- and glycine-receptors in CNS neurons is shaped by their relative expression levels. Brain Research. 2020;1748:147071.
15. Stephenson FA, Mukhopadhyay R. How the glycine and GABA receptors were purified. J Biol Chem. 2012;287(48):40835-7.
16. Kilb W. When Are Depolarizing GABAergic Responses Excitatory? Frontiers in Molecular Neuroscience. 2021;Volume 14 - 2021.
17. Burman RJ, Brodersen PJN, Raimondo JV, Sen A, Akerman CJ. Active cortical networks promote shunting fast synaptic inhibition in vivo. Neuron. 2023;111(22):3531-40.e6.
18. Dembitskaya Y, Kirsanov A, Wu Y-W, Brazhe A, Semyanov A. Spatiotemporal differences of GABAergic polarization and shunting during dendritic integration. bioRxiv. 2025:2025.04.05.647352.
19. Fishell G, Rudy B. Mechanisms of inhibition within the telencephalon: "where the wild things are". Annu Rev Neurosci. 2011;34:535-67.
20. Lipkin AM, Bender KJ. Axon Initial Segment GABA Inhibits Action Potential Generation throughout Periadolescent Development. J Neurosci. 2023;43(37):6357-68.
21. Terenzio M, Schiavo G, Fainzilber M. Compartmentalized Signaling in Neurons: From Cell Biology to Neuroscience. Neuron. 2017;96(3):667-79.
22. Nusser Z. Differential subcellular distribution of ion channels and the diversity of neuronal function. Curr Opin Neurobiol. 2012;22(3):366-71.
23. Galvan A, Kuwajima M, Smith Y. Glutamate and GABA receptors and transporters in the basal ganglia: what does their subsynaptic localization reveal about their function? Neuroscience. 2006;143(2):351-75.
24. Muller E, Le-Corronc H, Legendre P. Extrasynaptic and postsynaptic receptors in glycinergic and GABAergic neurotransmission: a division of labor? Front Mol Neurosci. 2008;1:3.
25. Yu H, Bai XC, Wang W. Characterization of the subunit composition and structure of adult

human glycine receptors. Neuron. 2021;109(17):2707-16 e6.
26. Vu ET, Krasne FB. Evidence for a computational distinction between proximal and distal neuronal inhibition. Science. 1992;255(5052):1710-2.
27. Malosio ML, Marqueze-Pouey B, Kuhse J, Betz H. Widespread expression of glycine receptor subunit mRNAs in the adult and developing rat brain. EMBO J. 1991;10(9):2401-9.
28. Avila A, Nguyen L, Rigo JM. Glycine receptors and brain development. Front Cell Neurosci. 2013;7:184.
29. Molchanova SM, Comhair J, Karadurmus D, Piccart E, Harvey RJ, Rigo JM, et al. Tonically Active alpha2 Subunit-Containing Glycine Receptors Regulate the Excitability of Striatal Medium Spiny Neurons. Front Mol Neurosci. 2017;10:442.
30. Ceder MM, Magnusson KA, Weman HM, Henriksson K, Andreasson L, Lindstrom T, et al. The mRNA expression profile of glycine receptor subunits alpha 1, alpha 2, alpha 4 and beta in female and male mice. Mol Cell Neurosci. 2024;131:103976.
31. Camuso S, Vella Y, Abadi SY, Mille C, Brône B, Specht CG. Identification of low copy synaptic glycine receptors in the mouse brain using single molecule localisation microscopy. bioRxiv. 2025:2025.01.07.631736.
32. Kreitzer AC. Physiology and pharmacology of striatal neurons. Annu Rev Neurosci. 2009;32:127-47.
33. McCutcheon RA, Abi-Dargham A, Howes OD. Schizophrenia, Dopamine and the Striatum: From Biology to Symptoms. Trends Neurosci. 2019;42(3):205-20.
34. Horvitz JC. Dopamine gating of glutamatergic sensorimotor and incentive motivational input signals to the striatum. Behav Brain Res. 2002;137(1-2):65-74.
35. Devoght J, Comhair J, Morelli G, Rigo JM, D'Hooge R, Touma C, et al. Dopamine-mediated striatal activity and function is enhanced in GlyRalpha2 knockout animals. iScience. 2023;26(8):107400.
36. Zhong S, Navaratnam D, Santos-Sacchi J. A genetically-encoded YFP sensor with enhanced chloride sensitivity, photostability and reduced ph interference demonstrates augmented transmembrane chloride movement by gerbil prestin (SLC26a5). PLoS One. 2014;9(6):e99095.
37. Lemmens V, Thevelein B, Vella Y, Kankowski S, Leonhard J, Mizuno H, et al. Hetero-pentamerization determines mobility and conductance of Glycine receptor α3 splice variants. Cell Mol Life Sci. 2022;79(11):540.
38. Bormann J, Rundström N, Betz H, Langosch D. Residues within transmembrane segment M2 determine chloride conductance of glycine receptor homo- and hetero-oligomers. Embo j. 1993;12(10):3729-37.
39. Krashia P, Lape R, Lodesani F, Colquhoun D, Sivilotti LG. The long activations of α2 glycine channels can be described by a mechanism with reaction intermediates ("flip"). J Gen Physiol. 2011;137(2):197-216.
40. Zhang Y, Ho TNT, Harvey RJ, Lynch JW, Keramidas A. Structure-Function Analysis of the GlyR α2 Subunit Autism Mutation p.R323L Reveals a Gain-of-Function. Front Mol Neurosci. 2017;10:158.
41. Yu H, Bai XC, Wang W. Characterization of the subunit composition and structure of adult human glycine receptors. Neuron. 2021;109(17):2707-16.e6.
42. Morris CE, Montpetit M. Multiple conductance states of the acetylcholine receptor channel complex. Can J Physiol Pharmacol. 1986;64(3):347-55.
43. Yelshanskaya MV, Patel DS, Kottke CM, Kurnikova MG, Sobolevsky AI. Opening of glutamate receptor channel to subconductance levels. Nature. 2022;605(7908):172-8.
44. Zhang J, Yuan H, Yao X, Chen S. Endogenous ion channels expressed in human embryonic kidney (HEK-293) cells. Pflügers Archiv - European Journal of Physiology. 2022;474(7):665-80.
45. Ullah G, Nosyreva ED, Thompson D, Cuello VA, Cuello LG, Syeda R. Analysis of pressure-activated Piezo1 open and subconductance states at a single channel level. J Biol Chem. 2024;300(4):107156.
46. Kolesnikov D, Perevoznikova A, Gusev K, Glushankova L, Kaznacheyeva E, Shalygin A. Electrophysiological Properties of Endogenous Single Ca2+ Activated Cl− Channels Induced by Local Ca2+ Entry in HEK293. International Journal of Molecular Sciences. 2021;22(9):4767.
47. Schrimpf W, Barth A, Hendrix J, Lamb DC. PAM: A Framework for Integrated Analysis of Imaging, Single-Molecule, and Ensemble Fluorescence Data. Biophys J. 2018;114(7):1518-28.

This text was supported by GenAI.

Acknowledgements – I would like to express my deepest appreciation to all those who provided me the possibility to complete this thesis. I am thankful to my daily supervisor, Yana Vella, for her patient guidance, continuous support, and invaluable insights throughout the entire research process. I would also like to thank Petra Bex, who taught me the patch-clamp technique and provided essential guidance during the single-channel recordings. Her expertise and encouragement were instrumental in my development. My appreciation also goes to my promotor, Prof. Dr. Bert Brône, for his constructive feedback and overall supervision. I am equally grateful to Andreea Burlacu and Amber Delbroek for their technical assistance, insightful discussions, and mental support along the way. I would like to thank the BIOMED – Biomedical Research Institute at UHasselt for providing the facilities, resources, and technical support that enabled me to carry out my experiments. I also acknowledge the Advanced Optical Microscopy Centre at Hasselt University for support with the microscopy experiments. Microscopy was made possible by the Research Foundation Flanders (FWO, project G0H3716N). Finally, I wish to thank my family for their encouragement and support throughout this journey.

Author contributions – YV and BB conceived and designed the research. AVB and YV performed experiments and data collection. AVB performed data analysis and statistics. AVB wrote the paper. YV carefully edited the manuscrip